Current Source Inverter-Based PV System with Enhanced Active Filtering Functionalities

Thomas Geury[1,2,3]*, Sonia Pinto*[2]*, and Johan Gyselinck*[3]

[1] *F.R.I.A. scholarship student, Email: thomas.geury@ulb.ac.be*

[2] *INESC-ID Lisboa, Instituto Superior Técnico (IST), University of Lisbon (ULisbon), Lisbon, Portugal, Email: soniafp@tecnico.ulisboa.pt*

[3] *BEAMS Energy, Ecole Polytechnique de Bruxelles, Université Libre de Bruxelles (ULB), Brussels, Belgium, Email: johan.gyselinck@ulb.ac.be*

Abstract: This paper proposes a three-phase Photovoltaic (PV) inverter, with Active Power Filtering (APF) capability, that allows for Maximum Power Point Tracking (MPPT) and a nearly unitary Power Factor (PF) in the connection to the Low Voltage (LV) grid. A single-stage Current Source Inverter (CSI), with an inductive DC link, connects the PV array to the three-phase grid for reduced cost and improved performances, and the MPPT algorithm controls directly the power of the PV array. Based on the power balance of the whole system, the grid current references are generated in a grid-synchronized *dq* frame allowing for the mitigation of low-frequency current harmonics introduced by a non-linear load connected at the Point of Common Coupling (PCC), without the need for additional measurements. Active damping is used to minimise filter losses and reduce the high-frequency harmonics that result from the semiconductors switching. Simulation and experimental results are presented in unloaded and loaded situations, and with varying irradiance, to confirm the active filtering, PF regulation and MPPT operate correctly.

1 Introduction

With the growing development of renewable energies, grid-connected Photovoltaic (PV) inverters are being increasingly used in domestic and industrial installations, usually connected to the Low Voltage (LV) or the Medium Voltage (MV)

grid. In this regard, generalised interest has arisen for new PV converter topologies with enhanced reliability and grid capabilities.

The system characteristics of PV inverters, influencing the choice of the topology, can be summarised as follows [1, 2]: matching the voltage level of the grid, nearly unitary Displacement Power Factor (DPF), Maximum Power Point Tracking (MPPT) or power tracking, low ripple on DC and AC sides using adequate filtering, reliability influenced by the filtering components and the stress on the switches, high efficiency, compactness by reducing the number of stages of the converter and minimising the filtering requirements, and low cost even though the inverter only represents a limited percentage of the total system cost [3].

According to international standards [4], PV inverters should minimise their harmonic impact on the grid while also guaranteeing nearly unitary Power Factor (PF). The standards in force for interconnecting distributed resources, for current harmonic limits for currents up to 16 A, and for PV systems connected to the utility interface are IEEE 1547 (2003), IEEE 61000-3-2, and IEC 61727 (THD $<$ 5 % and PF $>$ 0.9), respectively. Also, standards requiring the distributed generation units to support the grid are being developed. For instance, the standard VDE-AR-N 4105 is now applicable in Germany for low-voltage units and requires an active power reduction or reactive power support in case of over-frequency or voltage rise, respectively. However, these functionalities are not the target of this paper even though they are easily compatible with the power-controlled system developed.

In recent years, Power Quality (PQ) has become an important issue given the increasing number of non-linear loads connected to the LV grid. Solutions to overcome the limited possibilities of passive filtering include series and parallel Active Power Filters (APFs) [5]. They allow mitigating voltage and current harmonics, thus reducing the Total Harmonic Distortion (THD) and voltage imbalance, increasing PF, minimising losses, and improving overall grid performances.

In this context, PV inverters can be provided with enhanced functionalities as they are usually not used to their full potential [6]. The concept of using the PV inverter as an APF as well so as to deal with some PQ issues has received quite little attention in the literature; still, interesting solutions have been developed for single- and three-phase systems [7].

In [8–10], the grid current harmonics are mitigated with a single-phase Pulse Width Modulation (PWM) Voltage Source Inverter (VSI), using an additional DC/DC converter for MPPT while the MPPT is integrated in the single-stage inverter control in [11], regulating the DC bus voltage. The system in [10], although transformerless, has the clear disadvantage of requiring the measurement of the load currents.

In [12–16], the grid current harmonics are mitigated using a three-phase VSI. The solution proposed in [12] has the drawback of requiring the measurement of the distorted load currents. Also, the MPPT algorithm assumes that the voltage at Maximum Power Point (MPP) is nearly constant and known, which is generally not the case. In [13], which only presents simulation results, the MPPT is performed by controlling the DC bus voltage. The grid current references are then generated using the power balance of the system. In [14–16], a hysteresis current controller is used. Again,

[14] has the drawback of requiring the measurement of the load currents while experimental results are presented for the single-stage system developed in [15] only. In [16], the current imbalance can also be compensated, thanks to the four-wire connection including the use of the neutral.

The topology of the converter is chosen in function of the abovementioned system characteristics. The PV system proposed in this paper uses a single-stage Current Source Inverter (CSI), which has some advantages when compared to the most common VSI systems. In the former topology, the DC link current is filtered by an inductor for improved robustness and lifetime [17] compared to the electrolytic capacitor used in the latter, which is widely considered to be the least reliable component in PV systems [17, 18]. Also, the filtered DC link current is to be preferred for a PV application [17, 19], and the unidirectional current flow in a CSI removes the need for the series diode usually placed by the manufacturer at the output of the PV array in VSI systems [2]. The CSI acts as a voltage-step-up converter, which makes it easier to match the level of the grid voltages without the need for an additional conversion stage and with lower PV voltage [18–21]. The smallest admissible transfer ratio is 1.155 [2], and the MPPT voltage range is full as long as the maximum string voltage does not exceed the limit. For a single-stage VSI topology, however, the minimum DC voltage must be higher than the peak grid voltages, leading to safety issues [2] and limiting the MPPT voltage range. In order to widen the range and lower the minimum DC voltage, an additional step-up converter is needed, resulting in a two-stage topology with reduced reliability and potentially higher losses and cost [3, 17, 22]. In addition to that, the little energy storage on the DC side of CSIs is suited to three-phase topologies due to the constant power flow from the generator to the grid [2, 18]. In the VSI topology, the shoot-through issue also reduces the reliability of the system while it is a normal state of operation in the CSI-one [3, 19]. Also, the use of reverse-blocking Insulated Gate Bipolar Transistor (IGBT) switches would eliminate the series diode and therefore decrease the conduction losses of the CSI and improve the overall system efficiency. Even though these components are still expensive and uncommon, they are expected to become more familiar and accessible in the near future [2, 17].

This paper combines the functionalities of harmonics compensation, MPPT and unitary DPF using a single-stage CSI topology for a three-phase system. Even though the prices of the converter module in itself and the DC link filtering component are expected to be higher than for an equivalent two-stage VSI, the absence of a boost DC-DC converter would make it an overall cheaper alternative. No measurement of the non-linear load is required and active damping [23, 24] is added to the system in order to avoid stability problems in the grid-side filter and reduce the high-order harmonics and filter losses for better efficiency. Also, the power of the PV array is directly controlled and is used for MPPT, which is done inside the single-stage inverter, together with the PF control.

Simulation and experimental results confirm the proper operation of the proposed system.

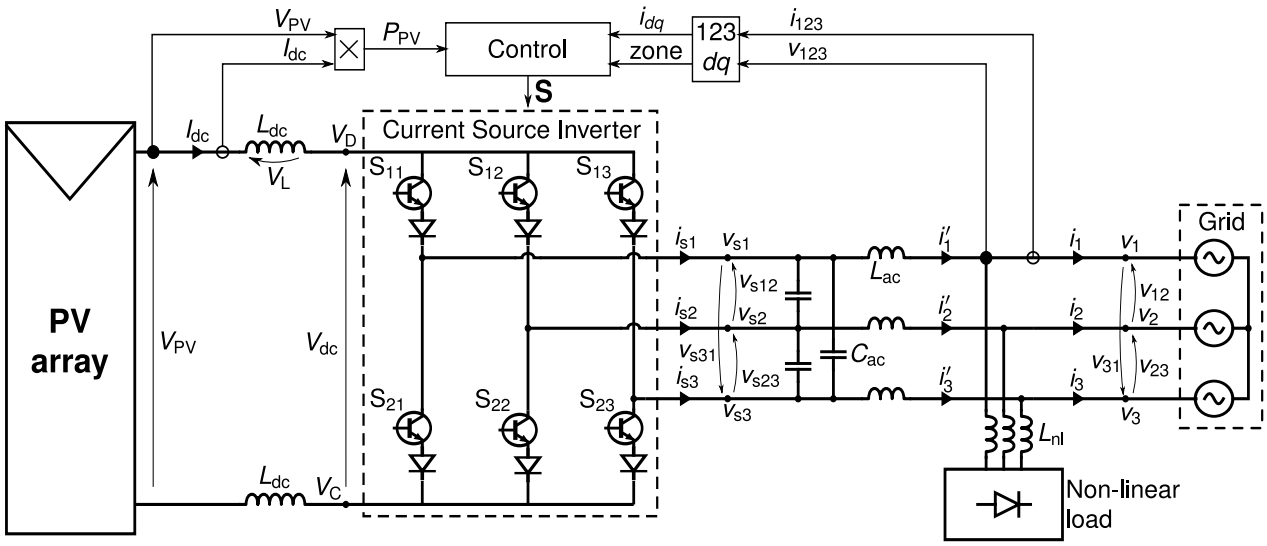

Fig. 1 *Complete three-phase single-stage PV system with a grid-connected CSI and a non-linear load*

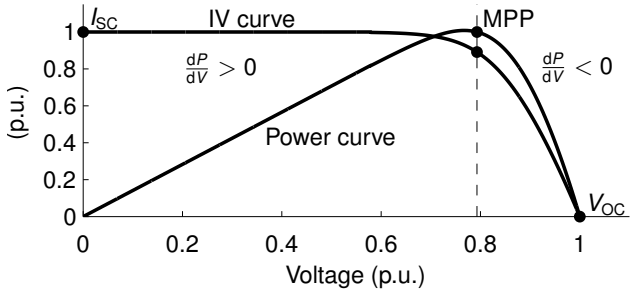

Fig. 2 *Characteristic curves of the PV array under rated conditions*

2 Description of the system

The complete three-phase single-stage PV system with a grid-connected CSI and a non-linear load connected at the Point of Common Coupling (PCC) is presented in Fig. 1 and is detailed in the next sections.

2.1 PV array

The PV array is modeled using the Single Exponential Model (SEM) of a solar cell, taking into account the influence of temperature and irradiance [25], with the voltage V_{PV} computed from the current I_{dc}. Fig. 2 displays the characteristic Current-Voltage (I-V) and Power-Voltage (P-V) curves of the PV array. These are delimited by three remarkable points, namely Short-Circuit (SC) (I_{SC}), Open Circuit (OC) (V_{OC}) and MPP (V_{MPP} & I_{MPP}).

2.2 Current Source Inverter

The DC/AC converter in Fig. 1 is made of six switches S_{kj}, $k \in \{1,2\}$, $j \in \{1,2,3\}$, each having a value S_{kj} of 1 when closed and 0 when open [26]. The states of the switches can be represented by the matrix

$$\boldsymbol{S} = \begin{bmatrix} S_{11} & S_{12} & S_{13} \\ S_{21} & S_{22} & S_{23} \end{bmatrix}. \tag{1}$$

Nine switching states are allowed since there should be strictly one switch conducting among the three upper ones, and one switch among the three lower ones to assure the continuity of the DC current and avoid short-circuiting the AC voltages, i.e. $\sum_{j=1}^{3} S_{kj} = 1, \quad k \in \{1,2\}$.

Based on (1), the relations between the AC and DC sides are the following:

$$\begin{bmatrix} V_{\mathrm{D}} \\ V_{\mathrm{C}} \end{bmatrix} = \boldsymbol{S} \begin{bmatrix} v_{\mathrm{s1}} \\ v_{\mathrm{s2}} \\ v_{\mathrm{s3}} \end{bmatrix}, \quad \begin{bmatrix} i_{\mathrm{s1}} \\ i_{\mathrm{s2}} \\ i_{\mathrm{s3}} \end{bmatrix} = \boldsymbol{S}^{T} \begin{bmatrix} I_{\mathrm{dc}} \\ -I_{\mathrm{dc}} \end{bmatrix}, \tag{2}$$

with $V_{\mathrm{dc}} = V_{\mathrm{D}} - V_{\mathrm{C}}$ and the grid-side currents directly obtained from the DC current. This is summarised in Table 1, where the grid currents are also represented as space vectors in the two-axis non-rotating frame $\alpha\beta$ using the Concordia transform [27]. In particular, vectors 7, 8 and 9 are null.

Table 1: Switching states of the DC/AC converter with the switches conducting on the upper **(1)** and lower **(2)** branches, with their effect on DC voltage and AC currents

S	**(1)**	**(2)**	V_{dc}	i_{s1}	i_{s2}	i_{s3}	$\|\vec{i_{\mathrm{s}}}\|$	$\arg(\vec{i_{\mathrm{s}}})$
1	S_{11}	S_{22}	v_{s12}	I_{dc}	$-I_{\mathrm{dc}}$	0	$\sqrt{2}I_{\mathrm{dc}}$	$-30°$
2	S_{12}	S_{21}	$-v_{\mathrm{s12}}$	$-I_{\mathrm{dc}}$	I_{dc}	0	$\sqrt{2}I_{\mathrm{dc}}$	$150°$
3	S_{12}	S_{23}	v_{s23}	0	I_{dc}	$-I_{\mathrm{dc}}$	$\sqrt{2}I_{\mathrm{dc}}$	$90°$
4	S_{13}	S_{22}	$-v_{\mathrm{s23}}$	0	$-I_{\mathrm{dc}}$	I_{dc}	$\sqrt{2}I_{\mathrm{dc}}$	$-90°$
5	S_{11}	S_{23}	$-v_{\mathrm{s31}}$	I_{dc}	0	$-I_{\mathrm{dc}}$	$\sqrt{2}I_{\mathrm{dc}}$	$30°$
6	S_{13}	S_{21}	v_{s31}	$-I_{\mathrm{dc}}$	0	I_{dc}	$\sqrt{2}I_{\mathrm{dc}}$	$-150°$
7	S_{11}	S_{21}	0	0	0	0	0	–
8	S_{12}	S_{22}	0	0	0	0	0	–
9	S_{13}	S_{23}	0	0	0	0	0	–

A three-phase LC grid-side filter is used to attenuate the CSI high-frequency switching harmonics [26], with the use of active damping for stability and minimization of filter losses (see Section 3.3), while two inductors L_{dc} are used in the DC link.

2.3 PV system dynamic model

In order to obtain the state-space equations of the system on the grid side, the state variables are identified: the grid currents i_1, i_2 and i_3, and the converter grid-side phase-to-phase voltages v_{s12}, v_{s23} and v_{s31}. Also, ideal grid voltage sources are considered:

$$v_i = \sqrt{2} V_{\text{rms}} \cos\left(\rho_v - (i-1)\frac{2\pi}{3}\right), \quad i = \{1,2,3\} \tag{3}$$

where $\rho_v = \omega_v t + \phi_v$ is determined by their constant pulsation ω_v and reference phase angle ϕ_v.

The equations for the grid currents and the converter grid-side phase-to-phase voltages are

$$\begin{cases} \dfrac{\mathrm{d}i_i}{\mathrm{d}t} = \dfrac{2}{3L_{\text{ac}}} v_{sij} + \dfrac{1}{3L_{\text{ac}}} v_{sjk} - \dfrac{1}{L_{\text{ac}}} v_i \\ \dfrac{\mathrm{d}v_{sij}}{\mathrm{d}t} = -\dfrac{1}{3C_{\text{ac}}}(i_i - i_j) + \dfrac{1}{3C_{\text{ac}}}(i_{si} - i_{sj}) \end{cases}, \tag{4}$$

with $(i,j,k) = \{(1,2,3),(2,3,2),(3,1,1)\}$, and where L_{ac} is the grid-side filter inductance, C_{ac} the grid-side filter phase-to-phase capacitance, and $i_{si}, \quad i = \{1,2,3\}$ are the converter grid-side currents.

Also, the dynamics on the DC side are ruled by the PV array characteristics in Fig. 2 and the inductor equation:

$$\frac{\mathrm{d}I_{\text{dc}}}{\mathrm{d}t} = \frac{1}{2L_{\text{dc}}} V_{\text{PV}} - \frac{1}{2L_{\text{dc}}} V_{\text{dc}}, \tag{5}$$

where V_{dc} is the voltage at the input of the converter and I_{dc} the current on the DC link.

To obtain a time-invariant state-space model of the PV system the Concordia-Park transform (6) is applied to (4), with each variable x modified according to $\begin{bmatrix} x_d & x_q \end{bmatrix}^T = \boldsymbol{T}^T \begin{bmatrix} x_1 & x_2 & x_3 \end{bmatrix}^T$.

$$\boldsymbol{T} = \sqrt{\frac{2}{3}} \begin{bmatrix} \cos\rho & -\sin\rho & \frac{1}{\sqrt{2}} \\ \cos(\rho - \frac{2\pi}{3}) & -\sin(\rho - \frac{2\pi}{3}) & \frac{1}{\sqrt{2}} \\ \cos(\rho - \frac{4\pi}{3}) & -\sin(\rho - \frac{4\pi}{3}) & \frac{1}{\sqrt{2}} \end{bmatrix}, \tag{6}$$

with ρ chosen equal to ρ_v. Thus, the state-space equations of the system in the grid-synchronized *dq* frame are

$$\begin{cases} \dfrac{\mathrm{d}i_d}{\mathrm{d}t} = \omega i_q + \dfrac{1}{2L_{\mathrm{ac}}} v_{\mathrm{sd}} + \dfrac{1}{2\sqrt{3}L_{\mathrm{ac}}} v_{\mathrm{sq}} - \dfrac{1}{L_{\mathrm{ac}}} v_d \\ \dfrac{\mathrm{d}i_q}{\mathrm{d}t} = -\omega i_d - \dfrac{1}{2\sqrt{3}L_{\mathrm{ac}}} v_{\mathrm{sd}} + \dfrac{1}{2L_{\mathrm{ac}}} v_{\mathrm{sq}} - \dfrac{1}{L_{\mathrm{ac}}} v_q \\ \dfrac{\mathrm{d}v_{\mathrm{sd}}}{\mathrm{d}t} = \omega v_{\mathrm{sq}} - \dfrac{1}{2C_{\mathrm{ac}}} i_d + \dfrac{1}{2\sqrt{3}C_{\mathrm{ac}}} i_q \\ \qquad\qquad + \dfrac{1}{2C_{\mathrm{ac}}} i_{\mathrm{sd}} - \dfrac{1}{2\sqrt{3}C_{\mathrm{ac}}} i_{\mathrm{sq}} \\ \dfrac{\mathrm{d}v_{\mathrm{sq}}}{\mathrm{d}t} = -\omega v_{\mathrm{sd}} - \dfrac{1}{2\sqrt{3}C_{\mathrm{ac}}} i_d - \dfrac{1}{2C_{\mathrm{ac}}} i_q \\ \qquad\qquad + \dfrac{1}{2\sqrt{3}C_{\mathrm{ac}}} i_{\mathrm{sd}} - \dfrac{1}{2C_{\mathrm{ac}}} i_{\mathrm{sq}} \end{cases}, \tag{7}$$

where the grid currents i_d and i_q, and the capacitor voltages v_{sd} and v_{sq} are the state variables; the converter grid-side currents i_{sd} and i_{sq}, and the grid voltages v_d and v_q are independent variables. This model will be further used to design the controllers of the PV system.

In the *dq* frame, the instantaneous power $p(t)$ and reactive power $q(t)$ are given by

$$\begin{cases} p(t) = v_d i_d + v_q i_q \\ q(t) = v_q i_d - v_d i_q \end{cases}. \tag{8}$$

Considering a reference frame synchronous with the grid voltages ($\rho = \rho_v$ in (6) and $\phi_v = 0°$), the grid voltages become time-invariant and are expressed by

$$\begin{bmatrix} v_d \\ v_q \end{bmatrix} = \begin{bmatrix} \sqrt{3}V_{\mathrm{rms}} \\ 0 \end{bmatrix}. \tag{9}$$

Therefore, the powers defined in (8) become

$$\begin{cases} p(t) = v_d i_d \\ q(t) = -v_d i_q \end{cases}, \tag{10}$$

where the variable i_d determines the instantaneous grid power and should be kept nearly constant for a constant power flow.

3 Control of the system

The control circuit of the system is presented in Fig. 3. The regulation of the PV power is used to generate the grid current references which aim at a unitary PF and current harmonics mitigation. The time-invariant state-space model of the system developed in the previous section is used to establish the grid current reference values.

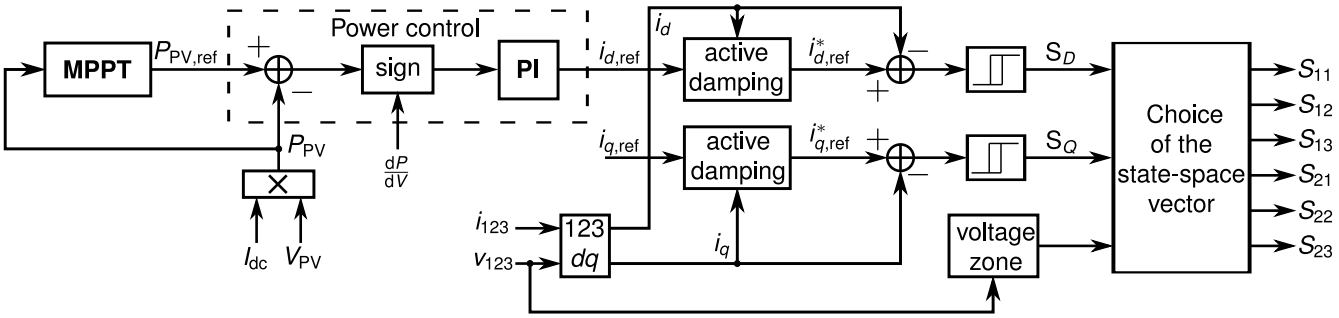

Fig. 3 *Control circuit of the complete system*

3.1 Sliding mode control of the grid currents

The *dq* components of the grid currents are controlled using sliding mode control [27, 28], which aims at providing the control laws for the power converter through variables S_D and S_Q. They constitute the necessary information for choosing the most adequate switching vector.

Considering the second-order grid-side filter, first-order sliding surfaces should be used for i_d and i_q [27–29]. The general expression for the surfaces is

$$S_{DQ}(e,t) = K_0\left(i_{dq,\text{ref}} - i_{dq}\right) + K_1\frac{\mathrm{d}}{\mathrm{d}t}\left(i_{dq,\text{ref}} - i_{dq}\right), \tag{11}$$

where K_0 and K_1 are positive-valued adjustable gains that affect the switching frequency of the converter, $e(t) = i_{\text{ref}} - i$ is the current error, and i_{dq} corresponds to the *d* and *q* components of the grid currents.

From (10), to guarantee a nearly unitary DPF, $i_{q,\text{ref}} = 0$. In order to mitigate the harmonics and have quasi-sinusoidal grid currents, the instantaneous power of the system defined in (10) should be controlled in addition to the control of the instantaneous reactive power through the variable i_q. This is done by controlling the current reference $i_{d,\text{ref}}$.

In order to verify the stability criterion $S(e,t)\dot{S}(e,t) < 0$, the time derivatives of the sliding surfaces are obtained [27], using the state-space equations (7):

$$\begin{aligned}\dot{S}_{DQ}(e,t) &= -K_0\frac{\mathrm{d}i_{dq}}{\mathrm{d}t} - K_1\frac{\mathrm{d}^2 i_{dq}}{\mathrm{d}t^2}\\ &= -K_0\left(\alpha\omega i_{qd} - \frac{1}{2\sqrt{3}L_{\text{ac}}}v_{sdq} + \alpha\frac{1}{2L_{\text{ac}}}v_{sqd} - \frac{1}{L_{\text{ac}}}v_{dq}\right)\\ &+ K_1\left(\left(\omega^2 + \frac{1}{3L_{\text{ac}}C_{\text{ac}}}\right)i_{dq} - \alpha\frac{\omega}{L_{\text{ac}}}v_{sqd}\right.\\ &\left.+\frac{\omega}{\sqrt{3}L_{\text{ac}}}v_{sdq} - \frac{1}{3L_{\text{ac}}C_{\text{ac}}}i_{sdq} + \alpha\frac{\omega}{L_{\text{ac}}}v_{qd}\right)\end{aligned}, \tag{12}$$

where $\alpha = 1$ for $S_D(e,t)$ and -1 for $S_Q(e,t)$. The only variables that can be directly controlled by the switching vector, at the output of the converter, are the currents i_{sd} and i_{sq}. Their modifications are applied to help meeting the stability criterion and should be high enough to affect the derivatives of the surfaces as required.

Using three- and two-level hysteresis comparators for i_d and i_q outputting the discrete variables S_D and S_Q, respectively, the conditions are:

- If $S_{DQ}(e,t) < 0$ then $S_{DQ} = 0$ and $\dot{S}_{DQ}(e,t) > 0$ is needed, i.e. i_{sdq} should be decreased
- If $S_D(e,t) \simeq 0$ then $S_D = 1$ and $\dot{S}_D(e,t)$ should not be significantly modified, i.e. i_{sd} should not be modified in average
- If $S_{DQ}(e,t) > 0$ then $S_{DQ} = 2$ and $\dot{S}_{DQ}(e,t) < 0$ is needed, i.e. i_{sdq} should be increased

Finally, the system is expected to guarantee a nearly unitary PF, through both the control of the DPF and the harmonics mitigation.

3.2 Space Vector Choice

The current space vectors defined in Table 1 are represented in Fig. 4a, where they also delimit the different voltage zones shown in Fig. 4b. These switching vectors can be applied to modify i_{sq} and i_{sd} in function of the discrete variables S_Q and S_D, respectively. In Fig. 4a, for instance, the voltages are in zone 2 (position of axis *d*); thus, the current vectors 2, 3 or 6 would increase i_{sq} while vectors 1, 4 and 5 would decrease it. When taking into account the control of both currents, the number of adequate switching combinations is reduced to 1; the results are shown in Table 2 which is used as a look-up table in the control circuit.

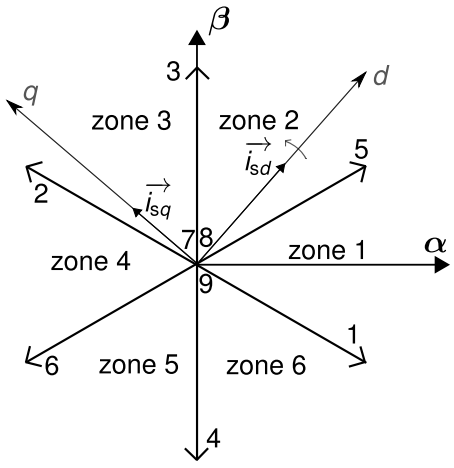

(a) *Space vectors of the converter output currents in the $\alpha\beta$ frame at the time of voltage zone 2, with the current space vectors (1 to 9, with the vectors 7, 8 and 9 being zero) delimiting the six voltage zones*

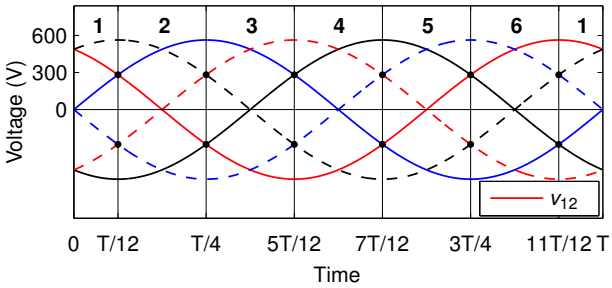

(b) *AC line-to-line voltages in the six voltage zones (maximum reached successively for $-v_{31}$, v_{23}, $-v_{12}$, v_{31}, $-v_{23}$, v_{12}, from left to right)*

Fig. 4 *Representation of the state-space vectors*

3.3 Active damping

A second-order filter with active damping is used for good attenuation of the switching harmonics while avoiding resonance and power losses [23, 24]. The method of virtual resistor is used, with a feedback of the inductor voltage, in order

Table 2: Switching vectors to apply to the converter in function of the sliding mode controls of i_q and i_d, i.e. in function of the discrete variables S_Q and S_D, and the voltage zone

		S_Q = **0**			S_Q = **2**		
	S_D	**0**	**1**	**2**	**0**	**1**	**2**
Zone	**1**	6	4	1	2	3	5
	2	4	1	5	6	2	3
	3	1	5	3	4	6	2
	4	5	3	2	1	4	6
	5	3	2	6	5	1	4
	6	2	6	4	3	5	1

to avoid extra measurements and components.

The single-phase equivalent block diagram of the system is presented in Fig. 5 where the current reference in the control is modified by the feedback of the grid-side filter inductor voltage v_l (full line). The modulator and converter are taken into account in the sizing and are approximated by the transfer function

$$G(s) = \frac{i_s(s)}{i^*_{ref}(s)} = Ge^{-sT_d} \simeq \frac{G}{T_d s + 1}, \tag{13}$$

where T_d, usually considered to be half the switching period $T_{sw} = 0.2\,\text{ms}$, is the average delay introduced by the converter between a control action on $i_{ref}(s)$ and the resulting value taken by $i_s(s)$ [23, 28], and G is the converter gain.

The inductor-voltage feedback gain $H(s)$ should be adjusted for the system to match the equivalent passive damping circuit, while removing the zero in the transfer function for a better attenuation of high frequencies. However, $H(s)$ is considered constant since no analytical match can be found between the two system transfer functions. In order to use the grid currents for feedback and avoid extra measurements (see the dotted line in Fig. 5), the grid-side filter inductor voltage is obtained with $v_l = sL_{ac}i$, resulting in new feedback gains for the grid currents:

$$K(s) = H(s)sL_{ac} = ksL_{ac}, \tag{14}$$

where k is a constant gain adjusted to 0.04 for a proper damping, and s is implemented as a discrete derivative. The derivative term cannot be avoided here if the grid currents are to be used for feedback and thus additional measurements avoided.

The active damping feedback is applied for both d and q components of the grid currents. In this approach, the cross terms due to dq components and the triangle connection of the grid-side filter capacitors are not considered [23, 24].

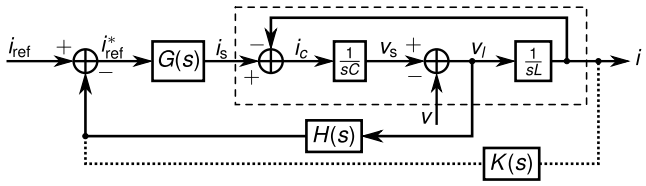

Fig. 5 *Block diagram of the single-phase equivalent system with active damping: feedback of the inductor voltage (full line) or the grid current (dotted line)*

3.4 Power control

The reference current $i_{d,\text{ref}}$, determining the power flow to the grid, directly influences the PV power P_{PV} and can thus be used to regulate it. In [13], where a VSI is used, this reference is obtained from a Proportional-Integral (PI) controller regulating the voltage V_{PV}; similarly, with a CSI, the DC link current could be regulated. However, in this work, it is the PV power itself which is input to the PI controller, as shown in Fig. 3, to generate the d component of the grid current reference.

3.4.1 PI controller

To control the power in the DC link and to establish the references for the grid currents, a PI controller is chosen:

$$C(s) = K_{\text{p}} + \frac{K_{\text{i}}}{s}, \tag{15}$$

where K_{p} and K_{i} are the proportional and integral gains, respectively, which are sized based on the block diagram of the system in Fig. 6. The modulator and converter are modelled similarly to (13), obtaining a transfer function that links the DC and AC sides of the system:

$$\frac{P_{\text{PV}}(s)}{i_{d,\text{ref}}(s)} = \frac{G_{\text{c}}}{1 + T_{\text{dv}}s}. \tag{16}$$

The time constant T_{dv} should be slower than the theoretical dynamics of the CSI module, i.e. the combination of the converter and grid-side filter, but faster than the grid dynamics [8] — it is here taken equal to 2.5 ms. The gain G_{c} is obtained using the power balance of the system, neglecting the losses:

$$P_{\text{PV}} \simeq i_d v_d \Rightarrow G_{\text{c}} = v_d, \tag{17}$$

where $v_d = \sqrt{3}V_{\text{rms}}$, from (9).

The system has two poles and one zero. The modulator and converter transfer function determines the location of one of the open-loop poles while the other one is zero due to the PI controller. Then, the controller gains can be varied to adjust the location of the zero and the closed-loop poles in the root locus of the system, aiming at stability and a fast step response. The resulting gains are $K_{\text{p}} = 0.05$ and $K_{\text{i}} = 0.2\,\text{s}^{-1}$.

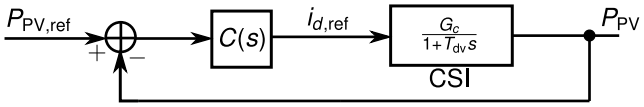

Fig. 6 *Block diagram of the power-controlled system*

Table 3: Influence of $^{dP}/_{dV}$ on the power balance of the system

S_D	V_{dc}[a]	V_L	I_{dc}	V_{PV}	$\frac{dP}{dV}$	i_d	P_{PV}
2	$> V_{PV}$	< 0	−	+	> 0	+	+
					< 0	+	−
0	$< V_{PV}$	> 0	+	−	> 0	−	−
					< 0	−	+

[a] See Table 1, Fig. 4b, and (5) for the relation between V_{dc} and V_{PV}.

3.4.2 Sign modification

The PI controller gains are sized considering that the instantaneous powers on the DC and AC sides are equal, with $i_q = 0$ on the grid. This implies that to increase P_{PV}, the reference current $i_{d,ref}$ is increased and thus the grid instantaneous power as well. This is verified as long as the system works in the zone where $^{dP}/_{dV} > 0$ in the power curve in Fig. 2. However, when $^{dP}/_{dV} < 0$, the same switching state of the CSI which makes V_{PV} either increase or decrease has an opposite effect on P_{PV}, as summarized in Table 3.

Thus, in the left zone of the power curve, $i_{d,ref}$ should be decreased to decrease P_{PV}, while in the right zone of the power curve, $i_{d,ref}$ should be increased to decrease P_{PV}. The solution is to modify the signal of the reference current by considering the sign of $^{dP}/_{dV}$ at the input of the PI controller.

3.4.3 Maximum Power Point Tracking

The most common MPPT methods control the PV voltage and current for VSI and CSI systems, respectively. However, as shown in the control circuit in Fig. 3, the active power produced by the PV array P_{PV} is here controlled. A simple and accurate algorithm is developed based on the perturb and observe principle common in MPPT methods, using three constant parameters—A, B and C—and the computational step Δt.

The MPPT algorithm outputs the reference $P_{PV,ref}(t+1)$ by comparing the previous reference $P_{PV,ref}(t)$ and the measured power $P_{PV}(t) = I_{dc}(t)\,V_{PV}(t)$. As shown in Fig. 7, the comparison results in 3 main cases:

1. In this case, the reference $P_{PV,ref}(t)$ is higher than the measured power P_{PV} by more than B. In general, it implies that the system is working at the MPP (the power cannot increase more) with an amplified ripple at the input of the PI

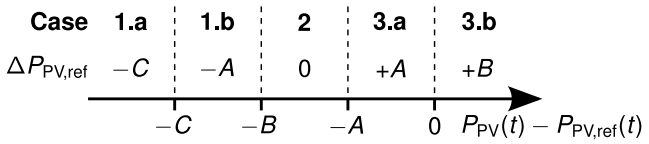

Fig. 7 *Different cases of the MPPT algorithm, with $C > B > A$ and $\Delta P_{\mathrm{PV,ref}} = P_{\mathrm{PV,ref}}(t+1) - P_{\mathrm{PV,ref}}(t)$*

controller that can distort the grid current reference. This is why the power reference is decreased in that case by a constant depending on the amplitude of the error. For instance, if the available maximum power suddenly drops, the error is large and the reference decreases by steps of $-C$ (case 1.a) to approach the new MPP. Thus, the maximum tracking speed in this case is $\left.{}^{\Delta P_{\mathrm{PV}}}/_{\Delta t}\right|_{\max} = {}^{-C}/_{\Delta t}\left[\mathrm{W\,s^{-1}}\right]$, considering an algorithm period Δt.

2. The second case corresponds to the steady state. In order to make sure that the MPP is reached, the reference is kept constant at a value higher than the measured power by a constant between A and B. If the power does not increase more, the MPP is reached. The ripple at the input of the PI controller is kept low by choosing relatively small constants A and B.

3. In this third case, the error is around zero and the reference needs to increase in order to try to raise the power. The reference increases by steps of A (case 3.a) or B (case 3.b), until the power reaches its maximum and case 2 is reached. Thus, the tracking speed for a power rise is given by $\left.{}^{\Delta P_{\mathrm{PV}}}/_{\Delta t}\right|_{\max} = {}^{B}/_{\Delta t}\left[\mathrm{W\,s^{-1}}\right]$.

In practice, due to the measurement errors, cases 1.b, 2 and 3.a can happen during steady state. Still, as the reference is always higher than the actual power in steady state, the accuracy is optimal and the real MPP is reached. The parameters A, B, C and Δt can be adjusted for specific MPPT requirements.

4 Results

The set-up presented in Fig. 1 was implemented in the laboratory using an isolation transformer in the connection to the grid, and simulated in the MATLAB/Simulink environment, using the parameter values listed in Table 4. As previously emphasised, the single-stage step-up converter limits the maximum voltage allowed at the output of the PV array and, in order to have a full voltage range for MPPT, the following condition applies: $V_{\mathrm{OC}} < \sqrt{3}\sin\frac{\pi}{3}\hat{v} = 254.5\,\mathrm{V}$. In order to optimise the system regarding cost and losses, the CSI should work at full amplitude modulation index with the PV array designed such that $V_{\mathrm{OC}} = 254.5\,\mathrm{V}$ [2]. That way, the installed semiconductor powers would be similar for this CSI topology and the two-stage VSI-one.

The experiments are performed using the fast-prototyping software and hardware dSPACE ds1103 and its ControlDesk interface. A PV emulator is used at the input of the converter and its parameters, such as the irradiance, can be varied on the ControlDesk interface. A programmable power supply—with maximum values of 1500 W, 360 V and 15 A—is used for this purpose. The results are taken at $V_{\mathrm{MPP}} \simeq 62.5\,\mathrm{V}$ and $I_{\mathrm{MPP}} \simeq 8\,\mathrm{A}$.

Table 4: Parameter values

Sym.	Description	Value	Units
T_s	Sample time	14	µs
v	Grid phase rms voltage	120	V
f_g	Grid frequency	50	Hz
P_{PV}	PV array nominal power[a]	500	W
V_{OC}	PV array OC voltage[a]	78.34	V
I_{SC}	PV array SC current[a]	9.08	A
L_{dc}	DC link inductance	12	mH
C_{ac}	Grid-side filter capacitance	10	µF
L_{ac}	Grid-side filter inductance	4	mH
P_{nl}	Non-linear load power	100	W

[a] It is taken at nominal atmospheric conditions, i.e. for an irradiance $G = 1\,\mathrm{kW/m^2}$ and a temperature $T = 25\,^{\circ}\mathrm{C}$.

Without load When no load is connected to the system, the full THD of the grid currents in simulation is 2.46 %, meeting the standard requirements. If only the first 40 harmonics are considered, thus removing the influence of the switching harmonics, $\mathrm{THD}_{40} = 2.17\,\%$. The latter confirms the proper operation of active damping and is used further on. The experimental grid currents are presented in Fig. 8a, with a THD of 4.47 % and a DPF of 0.965.

The measured efficiencies of the developed CSI system are presented in Fig. 8b, resulting in European and CEC efficiencies [4, 30] of 94.3 % and 94.1 %, respectively. The measured power losses, obtained as the difference between the input and output measured power, are shown as well. Also, for comparison purposes, the theoretical efficiencies and power losses [4, 30] were computed considering the characteristics of semiconductors and filtering components with the same ratings as the ones used in the laboratory. In this case, the computed European and CEC efficiencies are 95.4 % each. When considering the likely future trend of RB-IGBTs or a full amplitude modulation index, the efficiencies of this CSI system are similar to those obtained for different VSI-based topologies in [4, 22, 31].

With load The non-linear load connected at the PCC is reproduced using a full-bridge diode rectifier connected to the grid using three line inductances $L_{nl} = 13.1\,\mathrm{mH}$. The DC filtering capacitor is $C_{nl} = 440\,\mu\mathrm{F}$. The experimental load currents are particularly distorted and are shown in Fig. 9a with a load of $785\,\Omega$, resulting in an average voltage $V_{nl,0} = 280\,\mathrm{V}$, and consuming a power of 100 W. The THD is 80.42 % with particularly high 5^{th} and 7^{th} harmonics.

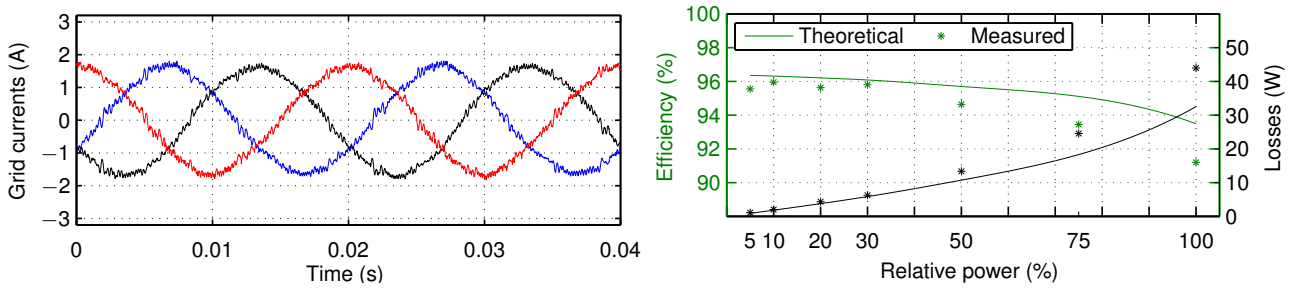

(a) *Experimental grid currents without load* – THD = 4.47 % **(b)** *Theoretical and measured efficiencies and power losses*

Fig. 8 *Results of the system operating in regular conditions*

The experimental grid currents with the non-linear load connected at the PCC and harmonics compensation are presented in Fig. 9b with a THD of 6.07 %. The 5^{th} and 7^{th} harmonics in particular are strongly attenuated to 1.3 % and 3 % of the fundamental, respectively. The compensation currents are presented in Fig. 9c while the grid current and voltage of phase 1 are shown in Fig. 9d to confirm that the DPF is nearly unitary. The converter output currents have a THD of 15.76 %, which is equivalent to that of the grid currents without active filtering. The simulation results in the same situation are also shown in Fig. 9. In particular, the THD of the grid currents is 3.59 % with a strong reduction of the 5^{th} and 7^{th} harmonics, the PF equals 0.999, and the results are similar to the experimental ones.

Also, in case the PV power is lower than the load power, the harmonics mitigation is still efficient such that sinusoidal grid currents supply the load.

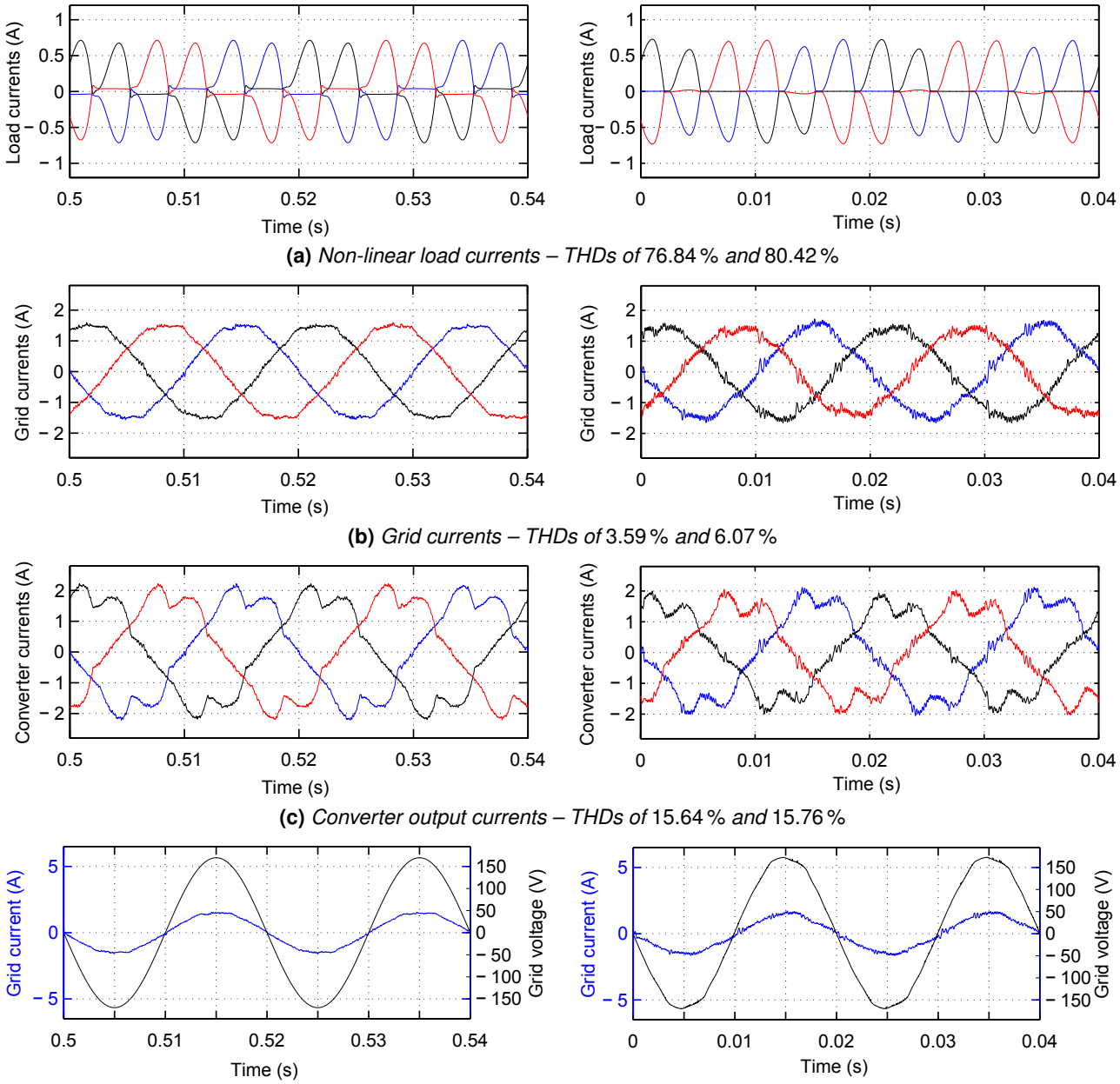

(a) *Non-linear load currents – THDs of* 76.84 % *and* 80.42 %

(b) *Grid currents – THDs of* 3.59 % *and* 6.07 %

(c) *Converter output currents – THDs of* 15.64 % *and* 15.76 %

(d) *Grid current* i_1 *and voltage* v_1 *– PF of 0.999 and 0.968*

Fig. 9 *Simulation (left) and experimental (right) results of the PV system in nominal conditions with a* 100 W *non-linear load connected at the PCC*

Varying irradiance The experiments are here performed by applying steps up and down of 0.1 kW/m^2 in the irradiance (between 0.9 kW/m^2 and 1 kW/m^2), i.e. power steps of approximately 50 W, to test the MPPT algorithm—the period Δt is 0.01 s and the constants A, B and C are equal to 0.5 W, 1 W and 25 W, respectively. The variables are recorded on an oscilloscope with a 4 W precision and without digital filtering.

Fig. 10a shows a succession of steps up and down to confirm the proper dynamics and operation of the MPPT algorithm. The zoom over the step up in Fig. 10b shows that the power reference increases by constant steps of amplitude B. Thus, approximately 50 MPPT periods of 0.01 s are necessary for a change of 50 W, as shown in the figure where the new MPPT is reached after approximately 0.5 s. A similar situation is shown in Fig. 10c for a step down: the reference is decreased by steps of value C, and the new MPP is tracked in a few time steps in order to limit the error with the actual power which cannot be higher than the maximum available power, no matter the reference.

The experimental results validate the system and the control strategy developed in this work. In particular, the harmonic content of the grid currents is reduced by more than half in the loaded situation and without load the THD of the grid currents is below the 5 % limit set in the standards [4].

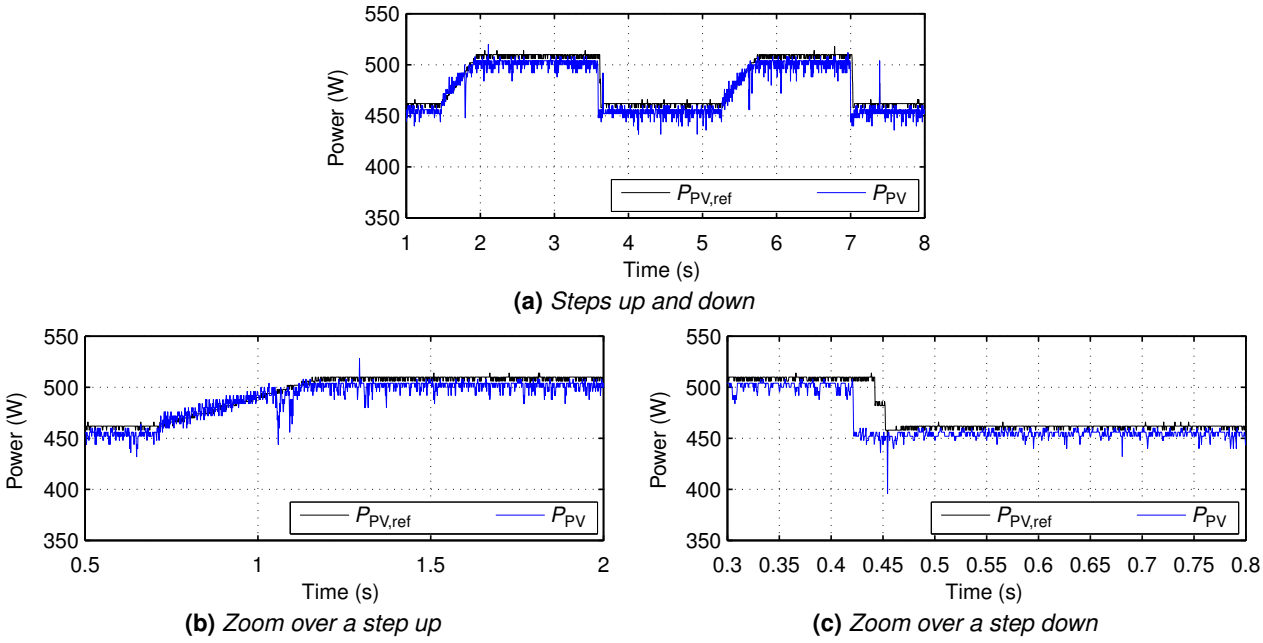

(a) *Steps up and down*

(b) *Zoom over a step up*

(c) *Zoom over a step down*

Fig. 10 *Experimental MPPT results of the PV power for steps of* 0.1 kW/m^2 *in the irradiance*

5 Conclusion

This research developed a CSI-based PV system that guarantees MPPT and unitary PF in the connection to the grid, and allows the capability of acting as an APF to mitigate grid current harmonics. The MPPT has been achieved controlling directly the power on the PV array, and the active power filtering capability is obtained without measuring the non-linear

load currents. Active damping has also been added to the control of the system to reduce the grid current switching harmonics and minimise losses. Simulation and experimental results confirm the system operates as expected in both dynamic and steady states: the non-linear load current harmonics are mitigated on the grid and the PV inverter tracks the maximum power with changing atmospheric conditions.

Aknowledgments

Thomas Geury would like to thank the Belgian Fund for training in Research in Industry and in Agriculture (F.R.I.A.) for the funding of this research project.

This work was supported by national funds through Fundação para a Ciência e Tecnologia (FCT) with reference UID/CEC/50021/2013.

References

1 Li, Q. and Wolf, P.: 'A review of the single phase photovoltaic module integrated converter topologies with three different DC link configurations', *IEEE Transactions on Power Electronics*, 2008, **23**, pp. 1320–1333.

2 Klumpner, C.: 'A New Single-Stage Current Source Inverter for Photovoltaic and Fuel Cell Applications using Reverse Blocking IGBTs'. Proc. *IEEE Power Electronics Specialists Conference*, 2007, pp. 1683–1689.

3 Zhou, Y., Huang, W., Zhao, P. and Zhao, J.: 'Coupled-inductor single-stage boost inverter for grid-connected photovoltaic system', *IET Power Electronics*, 2014, **7**, (2), pp. 259–270.

4 Teodorescu, R., Liserre, M. and Rodriguez, P.: *Grid converters for photovoltaic and wind power systems* (John Wiley & Sons, Ltd., 2011, 1st edn.), p. 398.

5 Khadem, S. K., Basu, M. and Conlon, M. F.: 'Parallel operation of inverters and active power filters in distributed generation system - A review', *Renewable and Sustainable Energy Reviews*, 2011, **15**, (9), pp. 5155–5168.

6 Hu, J., Zhu, J. and Dorrell, D.: 'Model predictive control of inverters for both islanded and grid-connected operations in renewable power generations', *IET Renewable Power Generation*, 2014, **8**, (3), pp. 240–248.

7 Patel, H. and Agarwal, V.: 'Investigations into the performance of photovoltaics-based active filter configurations and their control schemes under uniform and non-uniform radiation conditions', *IET Renewable Power Generation*, 2010, **4**, (1), pp. 12–22.

8 Pinto, S., Silva, J. and Lopes, S.: 'Smart microgeneration systems for power quality improvement', *International Review of Electrical Engineering (I.R.E.E.)*, 2011, **6**, pp. 2723–2735.

9 Fahmy, A. M., Ahmed, K. H., Hamad, M. S. and Adam, G. P.: 'Single-Phase Grid Connected Distributed Generation Interfacing Converter with Power Quality Improvement Capability'. Proc. *39th Annual Conference of the IEEE Industrial Electronics Society – IECON*, Vienna, 2013, pp. 2167–2172.

10 Lee, S.-W., Kim, J.-H., Lee, S.-R., Lee, B.-K. and Won, C.-Y.: 'A transformerless grid-connected photovoltaic system with active and reactive power control'. Proc. *IEEE 6th International Power Electronics and Motion Control Conference*, **3**, 2009, pp. 2178–2181.

11 Wu, T.-F., Nien, H.-S., Shen, C.-L. and Chen, T.-M.: 'A Single-Phase Inverter System for PV Power Injection and Active Power Filtering With Nonlinear Inductor Consideration', *IEEE Transactions on Industry Applications*, 2005, **41**, (4), pp. 1075–1083.

12 Schonardie, M. F., Ruseler, A., Coelho, R. F. and Martins, D. C.: 'Three-Phase Grid-Connected PV System With Active And Reactive Power Control Using dq0 Transformation'. Proc. *9th IEEE/IAS International Conference on Industry Applications*, São Paulo, Brazil, 2010.

13 Tumbelaka, H. H. and Miyatake, M.: 'Simple integration of three-phase shunt active power filter and photovoltaic generation system with Fibonacci-search-based MPPT'. Proc. *IEEE Symposium on Industrial Electronics and Applications*, Penang, 2010, pp. 94–99.

14 Blorfan, A., Wira, P., Flieller, D., Sturtzer, G. and Mercklé, J.: 'A Three-Phase Hybrid Active Power Filter with Photovoltaic Generation and Hysteresis Current Control'. Proc. *37th Annual Conference of IEEE Industrial Electronics Society – IECON*, Melbourne, 2011, pp. 4316–4321.

15 Marcos, V. Miñambres, Romero-Cadaval, E., Guerrero-Martinez, M. A. and Milanes-Montero, M. I.: 'Three-phase Single Stage Photovoltaic Inverter with Active Filtering Capabilities'. Proc. *38th Annual Conference of the IEEE Industrial Electronics Society – IECON*, 2012, pp. 5253–5258.

16 Archana, M. and Kondaiah, Y. C. V.: 'Grid Interfacing Inverter of Renewable Energy Sources to Improve the Power Quality in Distribution System', *International Journal of Advanced Research in Electrical, Electronics and Instrumentation Engineering*, 2012, **1**, (5), pp. 411–418.

17 Dash, P. P. and Kazerani, M.: 'Dynamic Modeling and Performance Analysis of a Grid-Connected Current-Source Inverter-Based Photovoltaic System', *IEEE Transactions on Sustainable Energy*, 2011, **2**, (4), pp. 443–450.

18 Sahan, B., Araújo, S. V., Nöding, C. and Zacharias, P.: 'Comparative Evaluation of Three-Phase Current Source Inverters for Grid Interfacing of Distributed and Renewable Energy Systems', *IEEE Transactions on Power Electronics*, 2011, **26**, (8), pp. 2304–2318.

19 Morsy, A., Ahmed, S. and Massoud, A. M.: 'Harmonic rejection in current source inverter-based distributed generation with grid voltage distortion using multi-synchronous reference frame', *IET Power Electronics*, 2014, **7**, (6), pp. 1323–1330.

20 Ho, B. M. T. and Shu-Hung Chung, H.: 'An Integrated Inverter With Maximum Power Tracking for Grid-Connected PV System', *IEEE Transactions on Power Electronics*, 2005, **20**, pp. 953–962.

21 Ertasgin, G., Whaley, N., Ertugrul, N. and SOONG, W.: 'A current-source grid-connected converter topology for photovoltaic systems'. Proc. *Australasian Universities Power Electronics Conference*, Melbourne, Australia, 2006.

22 Ahmed, M. E.-S., Orabi, M. and AbdelRahim, O. M.: 'Two-stage micro-grid inverter with high-voltage gain for photovoltaic applications', *IET Power Electronics*, 2013, **6**, (9), pp. 1812–1821.

23 Pan, D., Ruan, X., Bao, C., Li, W. and Wang, X.: 'Capacitor-Current-Feedback Active Damping With Reduced Computation Delay for Improving Robustness of LCL-Type Grid-Connected Inverter', *IEEE Transactions on Power Electronics*, 2014, **29**, (7), pp. 3414–3427.

24 Parker, S. G., Mcgrath, B. P. and Holmes, D. G.: 'Regions of Active Damping Control for LCL Filters', *IEEE Transactions on Industry Applications*, 2014, **50**, (1), pp. 424–432.

25 Villalva, M. G., Gazoli, J. R. and Filho, E. R.: 'Comprehensive approach to modeling and simulation of photovoltaic arrays', *IEEE Transactions on Power Electronics*, 2009, **24**, pp. 1198–1208.

26 Wheeler, P., Rodriguez, J., Clare, J., Empringham, L. and Weinstein, A.: 'Matrix converters: a technology review', *IEEE Transactions on Industrial Electronics*, 2002, **49**, pp. 276–288.

27 Pinto, S. and Silva, J.: 'Sliding mode direct control of matrix converters', *IET Electric Power Applications*, 2007, **1**, pp. 439–448.

28 Rachid, M. H.: *Power Electronics Handbook, Third Edition* (Elsevier Inc., 2011, 1st edn.), p. 1389.

29 Monteiro, J., Silva, J., Pinto, S. and Palma, J.: 'Linear and Sliding-Mode Control Design for Matrix Converter-Based Unified Power Flow Controllers', *IEEE Transactions on Power Electronics*, 2014, **29**, (7), pp. 3357–3367.

30 Femia, N., Petrone, G., Spagnuolo, G. and Vitelli, M.: *Power Electronics and Control Techniques for Maximum Energy Harvesting in Photovoltaic Systems* (Taylor & Francis Group, 2013, 1st edn.), p. 309.

31 Cho, Y.-W., Kim, K.-T., Cha, W.-J., Kwon, B.-H. and Lee, S.-H.: 'Evaluation and analysis of transformerless photovoltaic inverter topology for efficiency improvement and reduction of leakage current', *IET Power Electronics*, 2015, **8**, (2), pp. 255–267.